Available online at www.sciencedirect.com
SCIENCE DIRECT®
Journal of Nuclear Materials 342 (2005) 131–140
journal of nuclear materials
www.elsevier.com/locate/jnucmat

Vacancy dislocation loops in zirconium and their interaction with self-interstitial atoms

D. Kulikov [a], M. Hou [b,*]

[a] A.F. Joffe Physico-Technical Institute of RAS, Polytechnicheskaya Str. 26, 194021 St. Petersburg, Russia
[b] Physique des Solides Irradiés et des Nanostructures CP234, Université Libre de Bruxelles, Bd. du Triomphe, B-1050 Bruxelles, Belgium

Received 15 February 2005; accepted 12 April 2005

Abstract

The present work aims at predicting at the atomic scale, binding energies of vacancies to vacancy clusters in zirconium, preparing this way the modelling of their growth. Empirical laws established on the basis of simulation results are suggested, describing the size dependence of formation and binding energies of small voids (involving up to 1000 atoms) as well as basal, prismatic and pyramidal vacancy loops involving the same number of vacancies. The detailed atomic configurations of the loops are examined and characterized by means of areas where atoms are mis-coordinated and by strain fields. The importance of mis-coordinated areas is emphasized by an examination of self-interstitial atom (SIA) diffusion mechanisms in the vicinity of basal vacancy loops. The loops act as sinks for SIAs that, depending on the temperature, migrate one- or three-dimensionally to the mis-coordinated areas from which they cannot escape. By this mechanism, the annihilation of vacancy loops by SIA absorption is inhibited.

1. Introduction

Radiation damage evolution in materials is a complex process. It involves time scales from the femtosecond to years and spatial extents from the atomic volume to the cubic meter. It is also strongly material dependent. Much previous effort achieved in modelling damage evolution focused on metals used as structural materials in nuclear reactors. Among these materials, zirconium is of particular interest because of its use in fuel cladding. Zr differs from iron based materials because it exhibits a compact hexagonal structure. This has significant consequences on the mechanisms of defect growth in radiation environments, especially from the atomic to the micrometric scales at which point defects and point defect clusters play an important role. The radiation induced defects at these scales are cavities as well as vacancy and interstitial loops. Reviews of experimental understanding of defect evolution in radiation environment are available and significant efforts in theoretical understanding were and are still achieved, in particular, at the atomic scale [1–6].

In most aspects, the atomic scale in bulk materials is beyond experimental resolution. However, if atomic scale processes can be followed for a long enough time, they sum-up and lead to the nucleation and growth of voids and dislocation loops. These can be resolved by transmission electron microscopy once they become larger than a nanometer. Hence, if one succeeds in making damage predictions up to this stage of growth, it will be

* Corresponding author. Tel.: +32 2 650 5735; fax: +32 2 650 5227.
E-mail address: mhou@ulb.ac.be (M. Hou).

0022-3115/$ - see front matter © 2005 Elsevier B.V. All rights reserved.
doi:10.1016/j.jnucmat.2005.04.004

possible to check models for primary evolution against experimental observation.

Molecular dynamics (MD) is the natural technique for atomic scale modelling. Current systems sizes to which MD nowadays applies are of the order of hundreds of thousands of atoms and times of the order of nanoseconds. This allows the modelling of atomic collision cascades generated by energetic neutrons as well as groups of hundreds to thousands of vacancies and interstitials. Several reviews were published, synthesizing the understanding of radiation damage gathered in Zr and other hcp materials by MD [7–9], which encompass the evolution of collision cascades as well as the thermal diffusion properties of vacancies, interstitials and interstitial clusters. The lifetime of a collision cascade is no more than a few picoseconds. In contrast, the time needed for point defect clustering into voids or loops is orders of magnitude longer, in such a way that MD becomes unpractical and a multiscale approach necessary [10]. The longest point defect and cluster diffusion calculations in Zr by MD [11,12] lasted 100 ns. If the time was not sufficient to predict cluster growth, at least, it showed very clearly the temperature dependence of the diffusion anisotropy.

Object kinetic Monte Carlo simulations [13] allows the bridging of short and long time scales in systems of similar sizes as MD or larger. The method consists in sampling the kinetic path of defects as well as their reactions at random subject to Boltzmann statistics. This method requires an exhaustive list of the evolving objects and, in order to describe their reactions, a list of binding energies of each object to each other. Considering that some defects are more stable than others and that some are more mobile than others allows the list to be simplified. For instance, mono-interstitials and mono-vacancies are much more mobile than three-dimensional vacancy clusters. Therefore, the knowledge of their binding energy to clusters as a function of the cluster size is sufficient to model the cluster growth, and the list of binding energies can be replaced by a functional dependence on size. In addition, several cluster configurations are more stable than others as well, and their probability of occurrence is higher. Therefore, it may be expected pertinent only to retain the best stable ones in the list, although this approximation merits further critical investigation. This approach was already developed for Fe–Cu systems [14], as well as for vacancy clusters in Zr [15].

This work suggests the use of a population of vacancy cluster configurations for larger scale modelling. This population accounts for configuration fluctuations among the most stable ones of a given size subsequent to relaxation effects when one vacancy is added or released from that cluster. As it is shown in Section 3, at their present level of sophistication, cohesion models do not clearly predict whether small voids or small vacancy loops are more stable. However, both are seen experimentally in a radiation environment, in particular loops, probably as the consequence of the collapse of collision cascades and enhanced diffusion. For this reason, atomic configurations in the core of small vacancy loops (a few hundred atoms) and the related strain are characterized in Section 4. Mono-interstitials being the most mobile defects, their interaction with vacancy loops are then examined as a function of temperature. The results of this study are summarized in Section 5.

2. The molecular dynamics model

MD is used here for modelling zirconium crystals with point defects or groups of point defects and to extract the parameters needed as input for larger scale models. For sampling a kinetic path, the object kinetic Monte Carlo method uses as input: formation, migration and binding energies. Formation and binding energies may be predicted by MD directly, as well as migration energies in some simple cases.

The MD code we use, DYMOKA [16], is a modified version of the code CDCMD [17] developed to perform Metropolis Monte Carlo and classical MD modeling. Newton's equations of motion are integrated using a fifth order Gear predictor–corrector algorithm. The neighbour search is done through a linked cell method combined with a Verlet list [18]. This makes the CPU time per integration step fully linear with the number of atoms. The interatomic potential is tabulated and the interpolation of the potential tables is made through a 5th order Lagrange polynomial. The potential represents the core of the MD model and it is designed according to the second moment approximation scheme of the tight binding model, first suggested in [19], on the basis of Zr properties at equilibrium [20]. The range of this potential is beyond the third neighbour distance. Far from equilibrium, it requires corrections and one is suggested for describing close encounters as they occur in atomic collision cascades [21]. The separation distances involved in this work are of the order of the equilibrium first neighbour distance. Therefore, such a correction is ineffective in the context of this work. This potential was already used in earlier modelling of point defect clusters in Zr [22].

Simulations were performed at constant volume, using parallelepipedal boxes of hcp Zr with sizes from 100 000 atoms to 800 000 atoms, depending on the modelled void and loop sizes. Periodic boundary conditions are applied. For each specific calculation, the dimensions of the boxes were chosen large enough to avoid size effects on the results. The introduction of an isotropic defect (like a dislocation loop) induces an anisotropic strain. Therefore, the simulation boxes were always built with the largest extension in the direction of largest

strain range. In the case of dislocation loops, as shown in Section 5, it is perpendicular to the loop plane. This way, it is warranted that the atomic displacements due to relaxation around a defect are zero at the boundary of the box and the defect does not significantly interact with its image generated by the periodic boundary conditions. In what follows, the method for generating defects is described in the appropriate sections.

3. Formation and binding energies

Two main parameters governing the temporal evolution of vacancy dislocation loops and voids are their formation and binding energies. In previous work [14,15], a method based on a Metropolis Monte Carlo algorithm was developed allowing the evaluation of groups of vacancies and vacancies–impurities complexes. In [15], vacancy groups in hcp Zr were analysed and it was found that three-dimensional voids represent minimal energy configurations. The estimate was performed for groups of two to one thousand vacancies. These cavities are thus typically less than 5 nm diameter, which is, depending on temperature, one to two orders of magnitude smaller than the void and loop sizes currently observed as a consequence of irradiation [2]. In the present section, we calculate formation and binding energies of basal, prismatic and pyramidal dislocation loops involving the same number of vacancies as in [15] and the results are compared with those obtained for voids.

In order to calculate the binding energy of a vacancy to a dislocation loop, we proceed as follows. In a first step, neighbouring atoms are removed from one basal plane in order to form a basal loop, from two adjacent prismatic planes to form a prismatic loop or from two adjacent pyramidal planes to form a pyramidal loop. These configurations are annealed at constant temperature for several tens of picoseconds (typically 75 ps). The annealed configurations obtained are then quenched to 0 K before estimating the formation energy according to the relation:

$$E_f(N_V) = (N_0 - N_V) \cdot [E_c(N_V) - E_c], \tag{1}$$

where N_0 is the total number of atomic lattice sites in the box; E_c is the energy per atom of a relaxed Zr matrix containing a cluster of N_V vacancies in its lowest energy configuration, and E_c is the cohesive energy of pure hcp Zr.

In order to ensure that minimal energy is reached, the procedure is repeated using different annealing temperatures from 300 K to 900 K. In this procedure, and within the simulation times used, vacancy diffusion at the periphery of the loops is too slow to influence the annealed configurations obtained. On the other hand, accurate loop morphologies are unknown. Therefore, the procedure is also repeated using different initial morphologies. For vacancy prismatic and pyramidal loops, atoms are initially removed from within rectangles. For the basal loops, they are removed from triangular, rhombic, hexagonal and circular areas. The results are presented in Fig. 1. It is remarkable that formation energies display no systematic dependence on the initial configurations. Final configurations are also checked to ensure they are unaffected by the magnitude of the annealing temperature. Two dashed lines in Fig. 1 represent a lower and an upper bound to the formation energies obtained for basal loops. The dependence on the number of vacancies is

$$E_f^{max} = 4.3 * N_V^{0.7} \tag{2a}$$

and

$$E_f^{min} = 3.6 * N_V^{0.7}. \tag{2b}$$

The formation energies of three-dimensional voids having the same number of vacancies are systematically lower than formation energies of the three kinds of loops in the size range investigated. They are shown, in Fig. 1, to align with the following relation:

$$E_f^{Void} = 2.72 N_V^{2/3} \tag{3}$$

as already noted in [15].

The binding energy of one vacancy to an already existing group of vacancies is deduced from the formation energies according to [14,15]:

$$E_b(V) = E_f(\text{group}) + E_f(\text{vacancy}) - E_f(\text{group} + \text{vacancy}) \tag{4}$$

whether the group is a loop or a void.

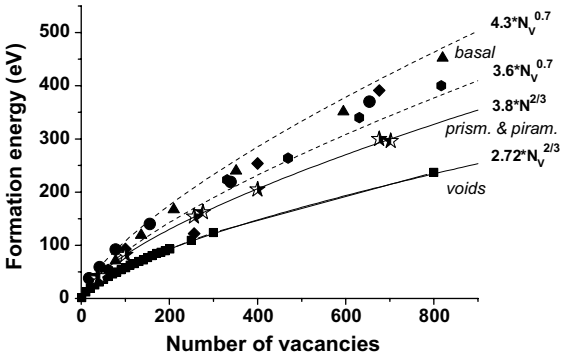

Fig. 1. The formation energies of different basal, prismatic and pyramidal vacancy dislocation loops vs. the number of vacancies forming them. The shapes of solid symbols represent the initial basal loop configurations: triangles, rhombs, hexagons and circles. Stars: formation energies of prismatic and pyramidal loops. Squares: 3D-voids. The limiting functions in Eq. (1) are represented by dashed lines, the fits for non-basal loops (Eq. (5)) and for voids (Eq. (2)) are given by solid lines.

Similarly to formation energies, limiting expressions can be found. For basal loops, we find

$$E_b^{min} = 1.78 + 4.3 * \{N_V^{0.7} - (N_V - 1)^{0.7}\} \quad (5a)$$

and

$$E_b^{max} = 1.78 + 3.6 * \{N_V^{0.7} - (N_V - 1)^{0.7}\}. \quad (5b)$$

These expressions are represented in Fig. 2. They are compared to the size dependence approximation of the binding energy of a vacancy to an existing void. A significant dispersion was found in [15] among this dependence and the standard deviation is also represented in Fig. 2. It is seen that, if one excepts the smallest loop sizes considered, binding energies fall inside the interval previously obtained for 3D clusters. For the smallest loops, Eq. (2), that are fitting functions, fail to be valid. This problem is discussed in [14].

The same procedure is now repeated for prismatic and pyramidal loops obtained by removing atoms from two adjacent $(1\bar{1}00)$ (prismatic) and $(10\bar{1}1)$ (pyramidal) planes, respectively. As far as the estimate of formation energies is concerned, quenching after high temperature annealing causes a technical problem in the case of prismatic loops as it is inefficient to relax long range thermally induced lattice distortions at large distances from the initial vacancy planes. Although these spurious distortions have no influence on the atomic rearrangement around the loop, they do have a large effect on the estimated formation energies. In this case, annealing is performed at 100 K and 50 K, taking care that the same loop configurations are found as with higher annealing temperatures. The formation and corresponding binding energy dependences on size are presented in Figs. 1 and 2, respectively, for comparison with those for loops in the basal plane and for three-dimensional voids. The results for prismatic and pyramidal loops align on the same function of the number of vacancies. It is seen that these loops are also less stable than voids and the binding energies of a vacancy to a loop is less than the binding energy to voids. The approximate expressions for the formation and binding energies for these loops are as follows:

$$E_f = 3.8 * N_V^{2/3}, \quad (6)$$

$$E_b = 1.78 + 3.8 * \{N_V^{2/3} - (N_V - 1)^{2/3}\}. \quad (7)$$

Although formation energies are lower than for basal loops, they are still higher than those of voids. Binding energies on the other hand are similar.

As an overall conclusion to this section, it is found that formation energies of small voids are systematically lower than those of loops. The extrapolation of the estimated fitting functions provides no indication for a change in this trend with larger numbers of vacancies. On the contrary, binding energies of loops and voids get closer as the number of vacancies get larger, indicating the possible coexistence of both, which is consistent with experiment [2].

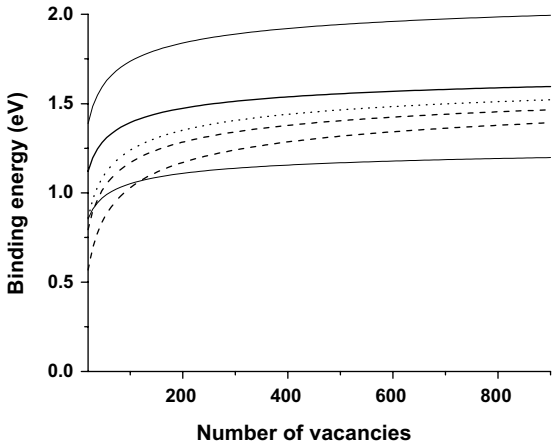

Fig. 2. Approximation functions for the binding energy of one vacancy to an already existing group of vacancies vs. the number of vacancies in that group. Dashed lines: limiting values for basal loops (Eq. (5)). Dotted line: prismatic or pyramidal loops (Eq. (6)). Thick solid line: voids; thin solid lines: standard deviation of the dispersion among the mean binding energies to voids.

4. Atomic configurations

The atomic configurations of three-dimensional vacancy clusters were already discussed in [15] and we focus here on vacancy loops.

For vacancy loops in the basal plane, two different types of relaxations were found. The first one, documented in the basic literature [23] and predicted in [24], is illustrated in Fig. 3 by comparing unrelaxed with relaxed configurations. The view is restricted to the central part of the MD box where a loop of hexagonal shape consisting of 469 vacancies is located. It was annealed at 600 K before quenching. Fig. 3(a) is a view parallel to the [0001] direction. It shows evidence of the displacement of atoms during annealing in one single basal plane. They are displaced to C lattice positions in the ABAB hcp stacking. In Fig. 3(b), which is a view parallel to a $[11\bar{2}0]$ direction, it is seen that most other atoms around the loop are displaced perpendicular to the basal plane i.e. along the [0001] direction. As a consequence, the atoms of all planes remain in their positions A or B in the stacking sequence of the hcp lattice, except the atoms in the one plane next to the loop that move to C positions. This is an extrinsic stacking fault which is sketched in Fig. 4. The stacking configuration was systematically examined for loops of various sizes, using different annealing temperatures, and representing as a whole a set of 36 different relaxation calculations. Such extrinsic

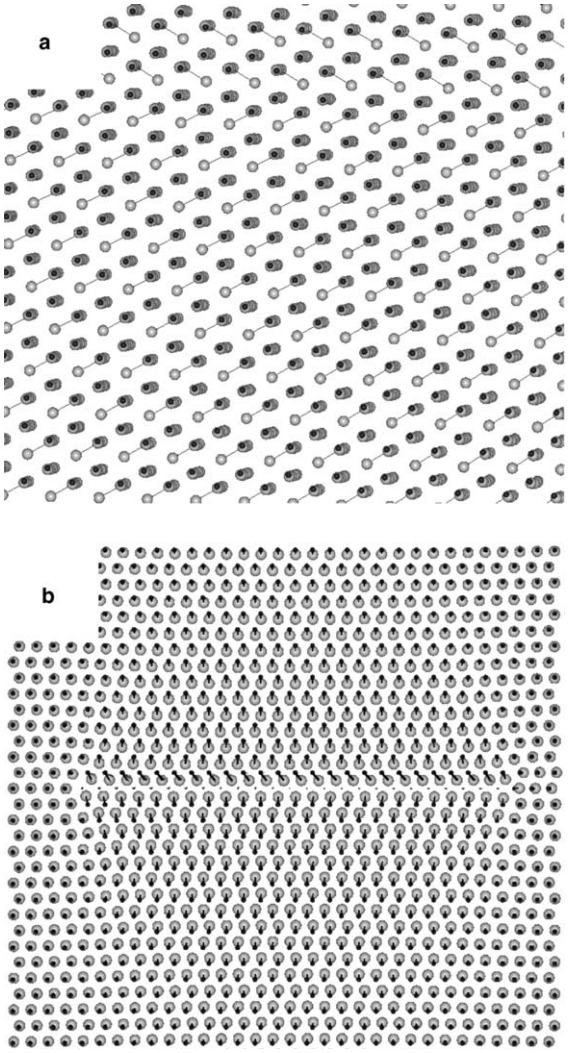

Fig. 3. Atomic configuration with an extrinsic stacking fault around the dislocation loop consisting of 469 vacancies in one basal plane, as obtained after annealing at 600 K: (a) projection along a [0001] direction; (b) projection along a $[11\bar{2}0]$ direction. The solid line segments represent the atomic displacements of individual atoms subsequent to annealing. In (a), only the atomic displacements in one plane are seen, from B to C sites (see text).

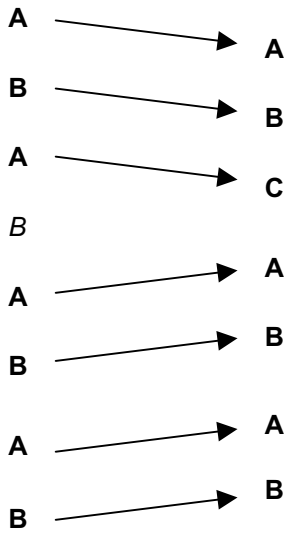

Fig. 4. Schematic view of the stacking sequence around the extrinsic basal vacancy dislocation loop, before relaxation on the left and after relaxation on the right. Italic *B* represents the plane from which atoms were removed in order to create a loop.

stacking faults were most often found for the smallest loops considered (less than 100 vacancies). This has already been predicted using a long range pair potential [24] rather than short range *N*-body potential as used here. In this latter work, it was found corresponding to the lowest basal stacking fault energy.

A second type of fault is found to dominate for larger loops, obtained at all annealing temperatures. It results from a larger displacement field with components in the $[11\bar{2}0]$ and the [0001] directions, extending over several interplanar distances. This is shown in Fig. 5 where two views of the dislocation loop are shown before and after annealing. In this example as in the former one, the loop is formed by 469 vacancies and the annealing temperature is 300 K. The stacking after annealing was identified and it is sketched in Fig. 6. The plane initially removed to create a loop is shown by an italic *A* in the initial stacking sequence. Starting from the upper part of the stacking represented in Fig. 6, one can see that the atoms are displaced from B toward C sites and from A toward B sites. The closer the atoms to the loop, the largest the displacements. Once passing the missing plane, the stacking changes. Atoms from B are displaced toward A sites and the atoms from A sites are displaced toward C. These displacements are represented by arrows in Fig. 6 and the underlined characters indicate the direction of atomic displacements. The size of the underlined symbols qualitatively shows the magnitude of displacements to the positions after annealing. This configuration is close, though not identical, to the intrinsic stacking fault dislocation loop in Zr documented in the basic literature [23].

The same views for atomic displacements are available for loops in prismatic and pyramidal planes. However, no simple picture allows us to describe the displacement fields in the cases of the relaxation of prismatic and pyramidal loops. Their range is larger than for loops in the basal plane and their geometry is hardly identified by 2D projection views as used in Figs. 3 and 5 for basal loops. A different approach must be used to characterize their structure, as described in the next section.

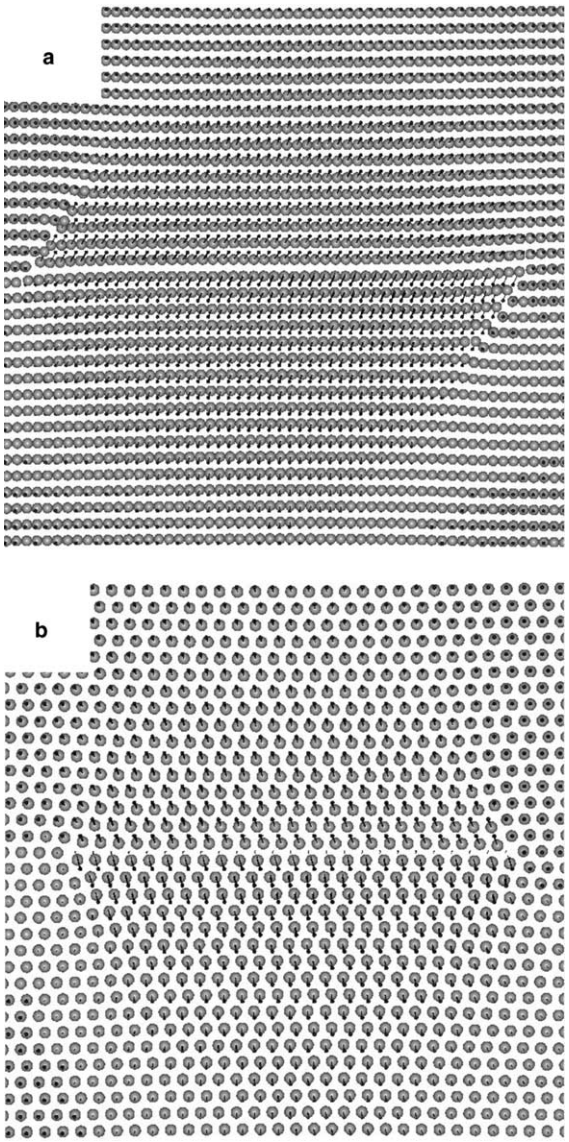

Fig. 5. Atomic configuration with an intrinsic stacking fault around dislocation loop consisting of 469 vacancies in one basal plane, as obtained after annealing at 300 K: (a) projection along a [1 0 1 0] direction; (b) projection along a [1 1 $\bar{2}$ 0] direction. The solid line segments represent the atomic displacements of individual atoms subsequent to annealing.

5. Spatial extent

Vacancy loops represent areas with locally lower density than the perfect crystal. As a consequence, mis-coordinated atoms are expected, that is, atoms with first neighbour coordination number different from the 12 of hcp, and strain field inhomogeneities. Both may help delineating the contour of the core of the loops. In addition, as is shown in the next section, mis-coordinated area and strain may play an important role in the diffusion of self-interstitials (SIA).

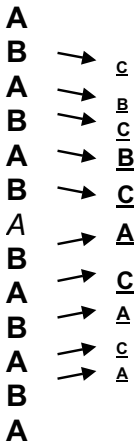

Fig. 6. Schematic view of the stacking sequence around the intrinsic basal vacancy dislocation loop. The initial stacking of (0 0 0 1) planes near the loop is shown on the left. The italic *A* stands for the plane from which atoms were removed in order to form the loop. On the right, the stacking is represented to which the configuration tends after annealing. The size of the symbols qualitatively represents the magnitude of the atomic displacements in each plane toward this configuration.

First neighbour coordination numbers of the atoms were mapped in the simulation box before and after loop annealing and quenching for the same loops as discussed in the previous section. The cores of the dislocation loops are always found surrounded by an area of mis-coordinated atoms. Because of the annealing, the inner loop area is always perfectly coordinated. Examples are given in the Fig. 7 for the two kinds of basal loops

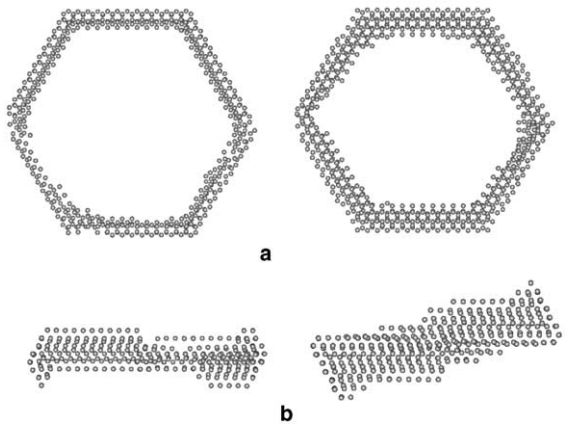

Fig. 7. Mis-coordinated atomic positions for both types of hexagonal basal loops after annealing ('extrinsic' loop on the left, 'intrinsic' loop on the right): (a) projection along (0 0 0 1); (b) projection along (1 1 $\bar{2}$ 0).

identified. The initial loop geometry is well mapped by mis-coordinated atoms. This mapping is only moderately affected by the kind of stacking, as seen by comparing the results for the two basal loop arrangements found in Figs. 3 and 5. The mis-coordinated area is a little broader in the case of the intrinsic fault and the annealing breaks its symmetry. The situation is more complex in the cases of prismatic and pyramidal loops. The mis-coordination maps are shown in Fig. 8. In the case of the prismatic loop, the annealing completely changes the morphology of the core which transforms from two- to three-dimensional and changes its axis of symmetry. Such a transformation also takes place for the pyramidal loop, but the effect is less pronounced.

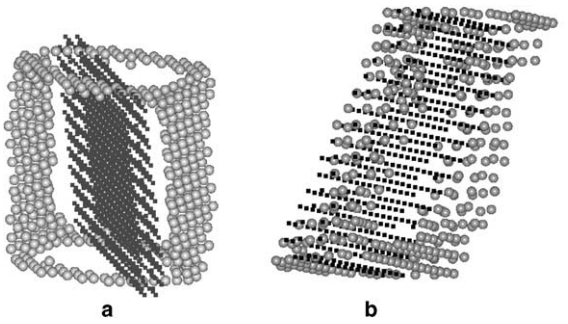

Fig. 8. Positions of mis-coordinated atoms: (a) prismatic loop, (b) pyramidal loop. In dark: mis-coordinated atomic positions before annealing; in grey: after annealing.

The combined effect of mis-coordination and lower local density inside vacancy loops is an inhomogeneous strain field, which may also be mapped. We measure the local strain at atom i according to the following expression:

$$S_i = \sum_j \frac{r_{ij} - r_0}{r_0}, \tag{8}$$

where r_{ij} is the distance between atom i and its first neighbour j, r_0 is the first neighbour distance in the perfect crystal at equilibrium and the summation runs over all first neighbours of atom i. With this definition, $S > 0$ corresponds to regions with tensile deformation while $S < 0$ for the regions under compressive deformation. In order to suppress background fluctuations in strain maps, we distinguish between compressive areas with $S < -0.03$, tensile areas with $S > 0.02$ and others where the strain is close to zero, namely, $-0.03 < S < 0.02$. Such maps are presented in Fig. 9 for the four kinds of loops considered. All maps are characterized by the occurrence of both tensile and compressive areas. In all cases, compressive surround tensile areas and the compressive–tensile interface closely maps the mis-coordinated areas. In the case of the basal loops (Fig. 9), no

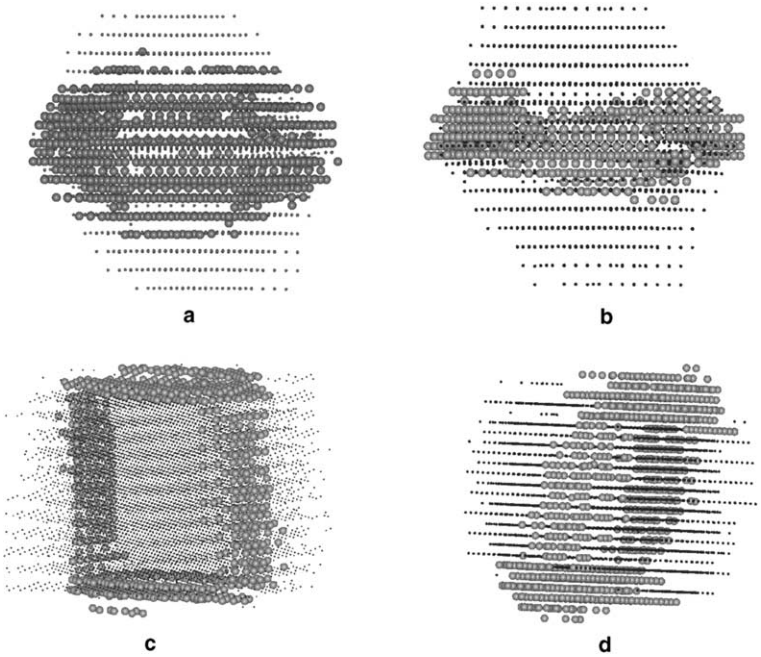

Fig. 9. The measure of strain S (Eq. (4)) for the four kinds of loops: (a) intrinsic; (b) extrinsic basal; (c) prismatic; (d) pyramidal. Light spheres: $S < 0$ (compression), dark points: $S > 0$ (tension). For the basal loops, projections are given along the $[1\bar{1}00]$ direction. For the prismatic and pyramidal loops, the viewing direction is selected to emphasize the complex three-dimensional nature of the strain distribution.

significant differences in the maps are found related to the extrinsic or intrinsic nature of the stacking fault. While compressive strain delineates the contour of the mis-coordinated area, the tensile area extends to longer range and in other directions, which is the signature of a shear deformation. As the strain field around the intrinsic basal defect is concerned, Fig. 9(b) shows that the loop plane is not a plane of symmetry. This is consistent with the relaxations sketched in Fig. 6. In the cases of prismatic and pyramidal loops and similarly to mis-coordination maps, due to the complex atomic rearrangement, the compressive area is three-dimensional and rotated as compared to the orientation of the unrelaxed loop plane.

6. Self-interstitial diffusion

Self-interstitial diffusion in a Zr perfect crystal was already the subject of a previous study [10,25]. Here, MD was employed to investigate this process using the same potential as in the rest of the present work. The results show different diffusion mechanisms in different temperature intervals. At low temperatures (200–500 K) the diffusion is mainly 1D, according to a $\langle 1\,1\,\bar{2}\,0\rangle$ crowdion mechanism (n atoms share $n-1$ lattice sites along a compact row and the defect propagates along this row). Direction changes in the basal plane happen with some jumps. When the temperature is increased, the probability of switching directions in a basal plane also increases and, above 500 K, some jumps take place outside this basal plane. When increasing the temperature further, 3D diffusion becomes more probable. However, as noted in [11], jumps in the basal plane remain more frequent than jumps out-of-plane.

We now turn to the issue of self-interstitial diffusion in the vicinity of a basal dislocation loop. Initially a circular loop consisting of 186 vacancies was created in a basal plane. Its diameter is close to 4.5 nm. It was annealed for 1–3 ps at 600 K and then quenched to allow atomic relaxation. As a consequence, an intrinsic defect configuration (see Fig. 6) was formed. The method for investigating the influence of this loop on diffusion is as follows. A basal crowdion, known as the equilibrium configuration of a self-interstitial [8,25] is created in the vicinity of the loop. Then the box, containing the loop and the interstitial was maintained at constant temperature for several tens of ps in order to identify the influence of a loop on interstitial diffusion trajectories. The parameters in this study are the temperature at which diffusion occurs, and the initial position of the crowdion with respect to the loop. Diffusion trajectories are calculated at 300 K, 600 K and 1450 K, covering this way the range from 1D to 3D diffusion in single crystals. Four cases are considered, each corresponding to a different location of the initial position of the basal crowdion in the vicinity of a loop. The first is at 6c-parameters (3 nm) from the centre of the loop along the [0 0 0 1] direction, the second at 3c-parameters (1.5 nm) from the centre of the loop in the same [0 0 0 1] direction, the third at the centre of the loop and the fourth in the plane of the loop at a distance of one loop diameter (4.5 nm) from its centre.

In the first case, at both 300 K and 600 K, 1D-diffusion takes place, parallel to the plane of the loop. This is illustrated in Fig. 10. In a perfect crystal, the frequency of direction changes in the same basal plane increases with temperature [11]. This is also found in the vicinity of the loop. However, in all cases observed in the present study, as shown in Fig. 10, the directional change takes place when the SIA passes 'above' the mis-coordinated area around the core. It happens either in the same basal plane or in the [0 0 0 1] direction toward the loop. In the latter case, the diffusion is also close to 1D (Fig. 10) but it stops as soon as the SIA reaches the mis-coordinated area where it remains trapped. Its motion in the [0 0 0 1] direction is fast, with an average velocity larger than one interplanar distance per picosecond ($\simeq$0.25 nm/ps).

At 1450 K, again as in perfect crystals, in the vicinity of the loop, the diffusion is 3D. However, it always leads to the recombination of the interstitial with the loop, in the mis-coordinated area. The total path is longer than in the case of 1D-diffusion along [0 0 0 1] at lower temperature and therefore, the time to become trapped is

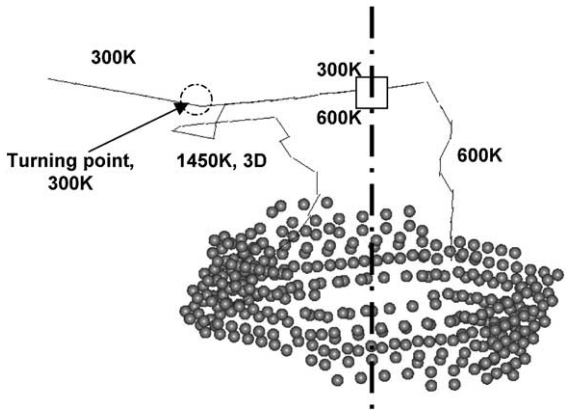

Fig. 10. Typical diffusion trajectories at different temperatures in the vicinity of an intrinsic basal loop. The initial position is marked by a square and the dot-dashed line is the axis of symmetry of the loop. At 300 K, diffusion is 1D along $\langle 1\,1\,\bar{2}\,0\rangle$ directions. The turning point shown is on a [0 0 0 1] row passing through the mis-coordinated area. The trajectory at 600 K is first 1D along $\langle 1\,1\,\bar{2}\,0\rangle$, then turns parallel to [0 0 0 1] toward the loop. The trajectory at 1450 K is 3D toward the loop and is confined within the cylindrical surface delimited by the mis-coordinated area. Trajectories at 600 K and 1450 K are trapped within the mis-coordinated area.

three times longer. The interstitial does not undergo any further diffusion jump and is undistinguishable from the other mis-coordinated atoms. A detailed study of high temperature diffusion trajectories shows that they consist of in-basal plane jumps separated by jumps from one basal plane to another. The former occur randomly, but are systematically confined in a cylinder whose section is delimited by the contour of the mis-coordinated area of the loop. The latter jumps, when they occur, are systematically directed toward the loop.

If the initial position of the interstitial is two times closer to the loop along the [0001] direction (i.e. 3c-parameters), in all cases trapping by the loop is observed within the mis-coordinated area.

We now turn to situations where the initial interstitial is located in the plane of the loop. When it is initially located at the centre of the loop, it systematically migrates along a $\langle 11\bar{2}0\rangle$ direction toward the mis-coordinated area where it is trapped. At 1450 K the repulsion between the two atoms forming the crowdion is observed sufficient to stimulate the 1D-diffusion of both in opposite directions. Both get trapped in the mis-coordinated area and a vacancy is left in the centre of the loop.

When the interstitial is initially located somewhere in the plane of a loop but outside, at a distance of one loop diameter (4.5 nm) from the centre, two cases are observed. Either trapping takes place (and this happens in most cases) and the migration of the interstitial is very quick (the average migration velocity is higher than 4 nm/ps), or, when the simulation is repeated with initial positions on a different $\langle 11\bar{2}0\rangle$ axis passing through the centre, the jump frequency is seen to drop strongly and is even prevented over a time of the order of 30 ps. Hence, depending on the position of the crowdion with respect to the loop, its diffusion can either be enhanced or prevented. This reflects the asymmetry of the mis-coordinated area and of the strain field with respect to a [0001] axis of the loop.

7. Conclusions

The results of this study can be summarized as follows:

(i) The formation energy of small voids is smaller than the formation energy of vacancy loops and no indication is found for a change of this trend at larger sizes. The formation energies of dislocation loops are only weakly dependent on their geometry and they are the same for prismatic and pyramidal loops.

(ii) It was shown in a previous study [14,15] that the binding energy of a vacancy to an already existing cluster of vacancies has a widespread distribution which is sensitive to the cluster configuration. The standard deviation of this distribution is given in Fig. 2 and it is found that the binding energy of vacancies to vacancy loops falls within this distribution in the size range investigated here.

(iii) Two kinds of basal loops are identified, qualified as extrinsic and intrinsic according to the literature, and characterized by different stacking sequences sketched in Figs. 4 and 6, respectively. Extrinsic stacking is the dominant configuration for the smallest loops (less than 100 vacancies, typically) while intrinsic stacking is dominant for the larger ones. The atomic configurations of prismatic and pyramidal loops are complex and involve displacement fields of larger spatial extent than basal loops.

(iv) The contour of the core of dislocation loops is conveniently mapped by mis-coordinated atoms. For basal loops, the mis-coordinated area is a torus in the basal plane which is not symmetric in the case of intrinsic stacking. It displays a 3D configuration in the core of prismatic and pyramidal loops. In the case of pyramidal loops, there is no straightforward relation with the planes from which vacancies were removed to form the loops.

(v) The strain field induced by the loop has a 3D extent which is confined by the mis-coordinated area. It is tensile in the perfectly coordinated area, and the compressive–tensile interface maps the mis-coordinated area.

(vi) Strain plays a significant role in the trapping of SIAs by vacancy loops. Trapping mechanisms in basal loops are temperature dependent. When trapping occurs, it is always in the mis-coordinated area and the trapped interstitials no longer diffuse, even at high temperature. The case where a large number of interstitials accumulate in this area is not considered here. It may result in a mechanical instability with the consequence of an overall rearrangement of the loop, which is not considered here. Depending upon temperature, as in perfect areas, the diffusion trajectories are 1D or 3D in the basal plane. However, a 1D-trajectory in the basal plane may be turned into a 1D-trajectory in the [0001] direction at some distance from the mis-coordinated area and the SIA is quickly trapped. Trapping by such a 1D mechanism at moderate temperatures (600 K in Fig. 10) is faster than the trapping by a 3D mechanism at higher temperature (1450 K in Fig. 10). A cylindrical surface delimited by the mis-coordinated area limits the spatial extent of 3D diffusion trajectories.

Further questions naturally arise beyond this contribution. Although there is no reason for the trapping of point defects in mis-coordinated areas to be specific to basal loops, a detailed study of the trapping by other loops and extended defects should be done as well as predictions of trapping efficiencies. Nb, which only differs from Zr by one atomic unit is known to form precipitates. The present results suggest that Nb may also be trapped at vacancy dislocation loops. However, with

the second moment tight binding as well as with standard EAM potentials, the molecular dynamics of Nb in Zr has no reason to differ from that of Zr in Zr. Since it is found to form precipitates and to influence the mechanical properties of the matrix, such potentials are certainly not sufficient to gather a full picture of the clustering of point defects, and the chemistry of the interaction between impurities and matrix atoms has to be accounted for. This pertains as well to other kinds of impurities. Nevertheless, it may be hoped that the information gathered at this stage on atomic scale configurations and mechanisms may be helpful to identify those that may have, at the microscale and macroscopic times, a sizeable influence on the evolution of microstructure in a radiation environment.

Acknowledgements

The authors are grateful to many colleagues for discussions and suggestions that determined the orientation of the present work. In particular, the idea of analysing loops in terms on mis-coordinated area and tensile/compressive strain maps was suggested by Charlotte Becquart, Christophe Domain and Alexandre Legris. R. Voskoboinikov made very useful comments on the modelling method of loops. This work was performed in the frame of the European thematic project SIRENA and the fruitful comments of all members of the project are highly appreciated. An additional financial support by Electricité de France (EDF) was determinant in the achievement of this work.

References

[1] D.O. Northwood, At. Energy Rev. (1977) 547.
[2] M. Griffith, J. Nucl. Mater. 159 (1988) 190.
[3] N. Christodoulou, A.R. Causey, R.A. Holt, C.N. Tomé, N. Badie, R.J. Klassen, R. Sauvé, C.H. Woo, in: E.R. Bradley, G.P. Sobol (Eds.), ASTM STP 125 (1996) 518.
[4] M. Griffiths, R.W. Gilbert, V. Fifleris, J. Nucl. Mater. 150 (1987) 159.
[5] M. Grifitths, H. Müllejans, Micron 26 (1995) 555.
[6] R.C. Pasianot, A.M. Monti, J. Nucl. Mater. 264 (1999) 198.
[7] D.J. Bacon, J. Nucl. Mater. 159 (1988) 176.
[8] D.J. Bacon, J. Nucl. Mater. 206 (1993) 249.
[9] C.H. Woo, J. Nucl. Mater. 276 (2000) 90.
[10] D.J. Bacon, Yu.N. Osetsky, Mater. Sci. Eng. A 365 (2004) 46.
[11] Y.N. Osetsky, D.J. Bacon, N. de Diego, Metall. Mater. Trans. 33A (2002) 777.
[12] N. de Diego, Y.N. Osetsky, D.J. Bacon, Metall. Mater. Trans. 33A (2002) 783.
[13] C. Domain, C.S. Becquart, L. Malerba, J. Nucl. Mater. 335 (2004) 121.
[14] D. Kulikov, L. Malerba, M. Hou, Philos. Mag., in press.
[15] D. Kulikov, L. Malerba, M. Hou, Nucl. Instr. Mehods B 228 (2005) 245.
[16] C.S. Becquart, K.M. Decker, C. Domain, J. Ruste, Y. Souffez, J.C. Turbatte, J.C. Van Duysen, Radiat. Eff. Def. Sol. 142 (1997) 9.
[17] A C version of CDCMD can be found at <http://www.ims.uconn.edu/centers/simul/index.htm#xmd>.
[18] M.P. Allen, D. Tildesley, in: Computer Simulation of Liquids, Oxford, Clarendon, 1987.
[19] F. Ducastelle, J. Phys. 31 (1970) 1055.
[20] G.J. Ackland, S.J. Wooding, D.J. Bacon, Philos. Mag. A 71 (1995) 553.
[21] D.J. Bacon, A.F. Calder, F. Gao, Radiat. Eff. Def. Sol. 141 (1997) 283.
[22] F. Gao, D.J. Bacon, L.M. Howe, C.B. So, J. Nucl. Mater. 294 (2001) 288.
[23] See e.g. N. Zabaras, <http://www.mae.cornell.deu/zabaras/Courses/MAE212/Lecture12>.
[24] V.G. Kapinos, Y.N. Osetsky, P.A. Platonov, J. Nucl. Mater. 195 (1992) 83.
[25] B.J. Whiting, D.J. Bacon, Mater. Res. Soc. Symp. Proc. 439 (1997) 389.